Towards Petascale DNS of High Reynolds-Number Turbulent Boundary Layer

Keegan R Webster

A thesis submitted in partial fulfillment of the requirements for the degree of

Master of Science in Aeronautics & Astronautics

University of Washington

2013

Reading Committee:

Antonino Ferrante

Mitsuru Kurosaka

Program Authorized to Offer Degree:
Aeronautics & Astronautics

University of Washington

Abstract

Towards Petascale DNS of
High Reynolds-Number Turbulent Boundary Layer

Keegan R Webster

Chair of the Supervisory Committee:
Assistant Professor Antonino Ferrante
Aeronautics & Astronautics

In flight vehicles, a large portion of fuel consumption is due to skin-friction drag. Reduction of this drag will significantly reduce the fuel consumption of flight vehicles and help our nation to reduce CO_2 emissions. In order to reduce skin-friction drag, an increased understanding of wall-turbulence is needed. Direct numerical simulation (DNS) of spatially developing turbulent boundary layers (SDTBL) can provide the fundamental understanding of wall-turbulence in order to produce models for Reynolds averaged Navier-Stokes (RANS) and large-eddy simulations (LES).

DNS of SDTBL over a flat plate at $Re_\theta = 1430 - 2900$ were performed. Improvements were made to the DNS code allowing for higher Reynolds number simulations towards petascale DNS of turbulent boundary layers. Mesh refinement and improvements to the inflow and outflow boundary conditions have resulted in turbulence statistics that match more closely to experimental results. The Reynolds stresses and the terms of their evolution equations are reported.

TABLE OF CONTENTS

Page

List of Figures ii

List of Tables v

Chapter 1: Introduction 1

Chapter 2: Mathematical Description 2
- 2.1 Governing Equations 2
- 2.2 Numerical Method 2
  - 2.2.1 Velocity Field Interpolation 4
  - 2.2.2 Computational Domain 5
- 2.3 Boundary Conditions 6
  - 2.3.1 Recycling/Rescaling Inflow 7
  - 2.3.2 Outflow Boundary Condition 10

Chapter 3: Results 13
- 3.1 Mesh Refinement 13
- 3.2 Reynolds Stresses 17

Chapter 4: Conclusions and Future Research 23

Appendix A: Reynold Stresses Verification 27

Appendix B: 2-D Domain Decomposition 33

Appendix C: Vortical Structures 35

LIST OF FIGURES

Figure Number | Page

2.1 Original configuration of the main (Code-B) and auxiliary (Code-A) simulations as shown in the paper by Ferrante & Elghobashi (2004a). 4

2.2 R_{11} contour on a $x_1 - x_3$ plane at $Re_\theta = 1430$ without reflection. . . . 8

2.3 R_{11} contour on a $x_1 - x_3$ plane at $Re_\theta = 1430$ with the inflow plane reflected. 8

2.4 R_{11} contour on a $x_1 - x_3$ plane with the inflow dynamically reflected. 9

2.5 Mean velocity profile (a) and velocity correlation (b) comparisons of the DNS code with dynamic reflection (Case C) to experiments by De Graaff & Eaton (2000) and DNS data by Schlatter *et al.* (2010) at $Re_\theta = 1430$. 10

2.6 Convective velocities for (2.8) and (2.9), denoted by the solid and dashed lines respectively 11

2.7 Reynolds number versus x for outflow boundary conditions (2.8) and (2.9), denoted by the solid and dashed lines respectively 12

3.1 Stream-wise velocity fluctuation correlation for DNS and experimental data by De Graaff & Eaton (2000). at $Re_\theta = 1430$ 13

3.2 $\langle u_1'^2 \rangle^+$ Reynolds stress for both experimental data by De Graaff & Eaton (2000) and DNS data. 14

3.3 Mean stream-wise velocity profiles comparison of experiments by De Graaff & Eaton (2000), the log-law $[\langle U \rangle^+ = \frac{1}{0.41}\log(z^+) + 5.2]$ and DNS data at two different Reynolds numbers. 15

3.4 Energy spectra for the stream-wise, span-wise and wall-normal directions with a fine and coarse mesh. 16

3.5 Total TKE budget comparison of the TBL code at $Re_\theta = 1430$ and 2900 as solid and dashed lines respectively. (a) Normalized as a function of z with the sum of the squares of the terms equal to one. (b) Normalized by the viscous scales. 19

3.6 The TKE budget comparison of the TBL code at $Re_\theta = 1430$ and 2900 as solid and dashed lines respectively. Normalized as a function of z with the sum of the squares of the terms equal to one. 20
3.7 The TKE budget comparison of the TBL code at $Re_\theta = 1430$ and 2900 as solid and dashed lines respectively. Normalized by the viscous scales. 21
3.8 Mean stream-wise velocity profiles at $Re_\theta = 1410$ and 2900 from left to right with experimental data from De Graaff & Eaton (2000) and the TBL DNS data. 22

A.1 Total TKE budget at $Re_\theta = 1410$. The TBL code (solid line) is compared to DNS data from Spalart (1988) (long-dash lines) and Schlatter *et al.* (2010) (short-dash lines). (a) Normalized as a function of z with the sum of the squares of the terms equal to one. (b) Normalized by the viscous scales. 27
A.2 The TKE budget at $Re_\theta = 1410$. The TBL code (solid line) is compared to DNS data from Spalart (1988) (long-dash lines) and Schlatter *et al.* (2010) (short-dash lines). Normalized as a function of z with the sum of the squares of the terms equal to one. 28
A.3 The TKE budget at $Re_\theta = 1410$. The TBL code (solid line) is compared to DNS data from Spalart (1988) (long-dash lines) and Schlatter *et al.* (2010) (short-dash lines). Normalized by the viscous scales. . . 29
A.4 Total TKE budget at $Re_\theta = 2540$. The TBL code (solid line) is compared to DNS data from Schlatter *et al.* (2010) (dashed line). (a) Normalized as a function of z with the sum of the squares of the terms equal to one. (b) Normalized by the viscous scales. 30
A.5 The TKE budget at $Re_\theta = 2540$. The TBL code (solid line) is compared to DNS data from Schlatter *et al.* (2010) (dashed line). Normalized as a function of z with the sum of the squares of the terms equal to one. 31
A.6 The TKE budget at $Re_\theta = 2540$. The TBL code (solid line) is compared to DNS data from Schlatter *et al.* (2010) (dashed lines). Normalized by the viscous scales. 32

B.1 Illustration of (a) 1-D domain decomposition and (b) 2-D domain decomposition Li (2013). 34

C.1 Coarse mesh vortical structures at $Re_\theta = 1430$ and 5200 with (512x256x96) and (2048x1024x512) meshes respectively 36

C.2 Vortical structures at $Re_\theta = 1430$ (1024x512x192) viewed from the (a) top, (b) side, (c) outlet and (d) looking upstream. 37

C.3 Hairpin vortices developing in a boundary layer at the transition region from laminar to turbulent flow (Perry *et al.* (1981)) 38

LIST OF TABLES

Table Number | Page

2.1 Computational domain dimensions. 6

2.2 Dynamic reflection parametric study 9

ACKNOWLEDGMENTS

I would like to thank my advisor Antonino Ferrante for his encouragement and mentoring throughout my graduate studies. Additionally, Darren Adams and David Bock from the National Science Foundation (NSF) ASTA team at NCSA for their computational support, allowing our code to run fast efficiently and create incredible visualizations. Thanks to Michael Dodd and Zhengcheng Gu for their collaboration on the TBL code. Furthermore, thanks to NSF (Award #1054591) for providing financial aid and computational resources. Simulations were run on Hyak and at the e-Science Institute of the University of Washington and Kraken at NICS of the University of Tennessee. As part of this research in collaboration with Michael Dodd and Antonino Ferrante, the paper Dodd *et al.* (2012) was presented at the 7th International Conference on Computational Fluid Dynamics.

DEDICATION

To my mother and father, for all their love and support throughout my education.

Chapter 1
INTRODUCTION

With rising fuel costs and greenhouse gas emissions, cleaner and more efficient vehicles are of increasing importance in today's society. These greenhouse gasses can largely be attributed to the CO_2 emissions of gasoline and diesel combustion engines and have a direct relation to global warming. Decreasing the fuel consumption of transportation vehicles will play a large role in our nation becoming carbon neutral. Skin-friction drag can be up to 60% of the total drag of flight vehicles, thus a large reduction of skin-friction drag on transportation vehicles will significantly improve their fuel consumption. In order to reduce skin-friction drag, it is essential to understand the physical mechanisms of turbulent boundary layers at high Reynolds number.

Due to major improvements in the affordability and speed of computers in the past two decades, computational fluid dynamics (CFD) is being widely used in both academia and industry in order to predict the behavior of turbulent flows. In industrial applications, the Reynolds number is typically too high for DNS to resolve all scales of turbulence in space and time. For industrial applications RANS simulations and more recently, LES, are commonly used. For LES, subgrid-scale models are needed to take into account the effects of the smallest scales below the LES cut-off length-scale. Without accurate subgrid-scale models, the overall accuracy and reliability of the simulation is greatly reduced.

The present work reports DNS results at $Re_\theta = 1430 - 2900$, the improvements made to the inflow and outflow boundary conditions, and is a first step towards petascale DNS of high Reynolds-number boundary layers ($Re_\theta = 10^4$).

Chapter 2

MATHEMATICAL DESCRIPTION

2.1 Governing Equations

Incompressible turbulent boundary layers are governed by the unsteady Navier-Stokes equations and the continuity equation, shown in non-dimensional form as equations 2.1 and 2.2:

$$\frac{\mathrm{D}U_j}{\mathrm{D}t} = -\frac{\partial p}{\partial x_j} + \nu \frac{\partial^2 U_j}{\partial x_k \partial x_k} \tag{2.1}$$

$$\frac{\partial U_j}{\partial x_j} = 0 \tag{2.2}$$

Where x_j represents the stream-wise (x), span-wise (y), and wall-normal (z) directions for $j = 1, 2, 3$ respectively. An in depth explanation of the governing equations can be found in the paper by Ferrante & Elghobashi (2004a).

In this paper '+' represents a quantity expressed in wall-units: $U^+_{ref} = U_{ref}/u_\tau$ and $z^+ = zu_\tau/\nu$ where the friction velocity $u_\tau = \sqrt{\tau_w/\rho}$ and τ_w is the wall shear stress. Brackets $\langle \cdots \rangle$ are used to represent the span-wise and temporal averaging of a quantity inside the brackets.

2.2 Numerical Method

"DNS of a spatially-developing turbulent boundary layer (SDTBL) requires the solution of the three-dimensional, unsteady Navier-Stokes and continuity equations with their prescribed initial conditions and the conditions on the six boundaries of the computational domain." (Ferrante & Elghobashi (2004a))

As discussed in the paper by Ferrante & Elghobashi (2004a) the generation of turbulent inflow is non-trivial. The inflow velocity components must satisfy the NS and continuity equations, making it one of the most complicated pieces of the DNS code. A separate simulation (Code-A) is needed that runs with the same domain size and time-step to create the initial velocity and pressure field and the inflow. Based on the work of Lund *et al.* (1998) for LES, Ferrante & Elghobashi (2004a) applied their methodology for turbulent inflow generation to DNS of SDTBL.

The method of Lund *et al.* (1998) first needs an auxiliary simulation referred to as Code-A. Shown in Fig. (2.1), the velocity field at the recycling plane is first rescaled and then copied as the inflow plane. The rescaling is done for the stream-wise and vertical components of the mean velocity as well as the velocity fluctuations in all three spatial dimensions. At $0.5L_x$ the mean velocity and velocity fluctuations at each time step are saved to be used as the turbulent inflow for the main simulation referred to as Code-B. The inflow method of Ferrante & Elghobashi (2004a) runs twice with two separate inflow conditions, which are referred to as Task-1 and Task-2.

In the first run of Code-A (Task-1) a turbulent kinetic energy spectrum, $E(K)$, is prescribed along with the wall normal profiles of the velocity correlation $\langle u_1^2 \rangle$, $\langle u_2^2 \rangle$, $\langle u_3^2 \rangle$ and $\langle u_1 u_3 \rangle$ at the inflow plane. Once Task-1 has run long enough to reach a turbulent state, the three-dimensional velocity field is used as the initial conditions of Task-2.

Task-2 implements the rescaling method from Lund *et al.* (1998) to re-size $\langle U_i \rangle$ and $\langle u_i u_j \rangle$ from the recycling plane to the inflow plane. The velocities and correlations are rescaled to match the growth rate of the SDTBL based on the boundary layer thickness Reynolds number, Re_δ, at the inflow plane.

Code-B inflow is generated by saving the velocities for Task-2 at the middle of the domain at every time iteration and copied as the inflow plane for Code-B. The initialization of velocity field uses the first inlet plane at $t = 0$ and copies it to all other planes and adds a random fluctuation less than or equal to 10% of $u_i(x = 0, y, z)$. The code is run until the flow is statistically stationary around $t = 150 \simeq 2600\nu/u_\tau^2$. From $150 \leq t \leq 300$ the statistics are calculated every ten time steps. The methodology for Task-1, Task-2 and Code-B are described in depth in the paper by Ferrante & Elghobashi (2004a). The method has been modified since the 2004 publication and the improvements will be discussed the following sections.

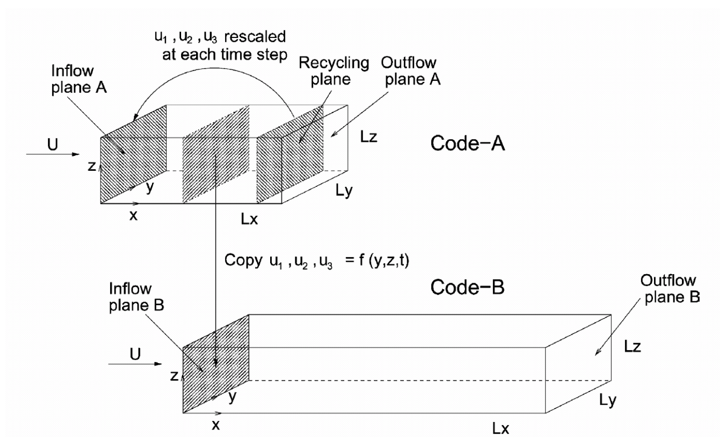

Figure 2.1: Original configuration of the main (Code-B) and auxiliary (Code-A) simulations as shown in the paper by Ferrante & Elghobashi (2004a).

2.2.1 Velocity Field Interpolation

At high Reynolds numbers, Task-1 becomes increasingly more difficult to perform as it required the number of processors to be divisible by not only the number of grid points in the span-wise direction, but in the wall-normal direction as well. This significantly limits the number of processors that can be used for the simulation. So much that at $Re_\theta = 5200$ with a six billion point mesh, Task-1 is impractical and would take weeks to run on 6144 cores. The solution is to remove Task-1 from the code entirely.

Task-2 would still need an initialized velocity field containing the turbulent kinetic energy spectrum and the turbulent velocity and velocity correlation profiles, but a new method to generate this field is needed. The new method takes a velocity field from a lower Reynolds number and interpolates the velocities over the finer mesh of the higher Reynolds number simulation. This was tested by taking a coarse $Re_\theta = 1430$ simulation and interpolating into a finer mesh $Re_\theta = 2900$ simulation. Comparing the statistics with and without Task-1 showed that the turbulent statistics were preserved with the new initialization.

Removing Task-1 from $Re_\theta = 2900$ saved $75,000$ CPU hours. At $Re_\theta = 5200$, the computational savings would be hundreds of thousands of CPU hours. Currently the interpolation is only in the stream-wise and span-wise directions, but in the future the code will interpolate in all three spatial dimensions.

2.2.2 Computational Domain

Another modification to the TBL code was the combining of Task-2 and Code-B into one simulation to save computational hours. Originally Task-2 ($L_x = 10\delta_0$) and Code-B ($L_x = 20\delta_0$) were used as seen in Fig. 2.1. The new simulation uses a single long box of $L_x = 30\delta_0$ which generates inflow from the recycling/rescaling of Task-2 and is long enough to take statistics sufficiently far away from the recycling plane. This eliminates the need to store and read the inflow plane generated by Task-2 for Code-B, saving computational storage space and reducing the computational time by half.

The dimensions and the number of grid points for Code-A and Code-B are provided in Table 2.1 for $Re_\theta = 1430$. The mesh is stretched in the wall normal direction with $z^+_{min} = 0.58$ and $z^+_{max} = 34$ to capture the smallest eddies within the boundary layer.

L_x	L_y	L_z	N_x	N_y	N_z	Δx^+	Δy^+	z^+_{min}
$30\delta_0$	$5\delta_0$	$3.6\delta_0$	768	256	96	14	7	0.58

Table 2.1: Computational domain dimensions.

2.3 *Boundary Conditions*

The span-wise boundary conditions are treated as periodic for both velocity and pressure. At the wall is a no-slip boundary condition for the velocity and a zero pressure gradient in the wall normal direction:

$$u_1 = u_2 = u_3 = 0, \frac{\partial p}{\partial z} = 0 \text{ at } z = 0. \tag{2.3}$$

The free-stream boundary has a stress-free Neumann condition for the the velocity and a Dirichlet condition for the pressure:

$$u_1 = 0, \frac{\partial u_2}{\partial z} = \frac{\partial u_3}{\partial z} = 0, p = 0 \text{ at } z = L_z \tag{2.4}$$

The outflow and inflow boundary condition have a zero pressure gradient in the stream-wise direction. The velocity at the outlet is calculated by the following differential equation:

$$\frac{\partial u_j}{\partial t} + U_c \frac{\partial u_j}{\partial x} = 0, \frac{\partial p}{\partial x} = 0 \text{ at } x = L_x. \tag{2.5}$$

U_C is the mean convective velocity at the exit plane. A more detailed explanation of the boundary conditions can be found in the paper by Ferrante & Elghobashi (2004a). Improvements to inflow and outflow boundary conditions are described in the following subsections.

2.3.1 Recycling/Rescaling Inflow

The recycling/rescaling inflow plane from Lund *et al.* (1998) was found to generate spurious two-point velocity correlations,

$$R_{ij}(r,x,t) = \langle u_i(x,t)u_j(x+r,t)\rangle, \tag{2.6}$$

at the recycling plane as shown in Fig. 2.2 for R_{11}. The spurious correlations can be seen at $x = 8.25$ and 16.5, multiples of the recycling plane location $x = 8.25$. The correlation at $x = 16.5$ is smaller, but still clearly visible. Using this inflow generation method, the stream-wise length L_x would have to be significantly increased to decorrelate the flow. This solution is impractical. An alternate solution was proposed by Morgan *et al.* (2011) for LES to dynamically reflect the recycled plane before copying as the inflow plane.

The periodic boundary conditions in the span-wise direction makes this reflection possible. A single reflection of the inflow plane does not remove the correlations. The result is in a diagonal correlation at $x = 8.5$ and a R_{ij} correlation at $x = 16.5$ as the flow is reflected a second time. This can be seen in Fig. 2.3, where the first spurious correlation disappears (diagonal correlation) and the second remains. In order to remove these correlations as well as temporal correlations the methodology described in Morgan *et al.* (2011) prescribes a dynamic reflection of the inflow plane. Meaning that at random time intervals the inflow plane is reflected about a random span-wise location.

A parametric study was conducted to find the optimal random reflection time constrains. The time interval needed to be as long as possible to preserve the vortical structures, but short enough to remove the correlation. The test parameters are shown in Table 2.2, where λ_{rfl} is defined as the characteristic stream-wise streak length (Morgan *et al.* (2011)). The time scale of the stream-wise streaks can be derived from λ_{rfl} as $\tau_{\text{rfl}} = \frac{\lambda_{\text{rfl}}}{0.8U_\infty}$.

The best results were from case (c), which produced the velocity correlation seen

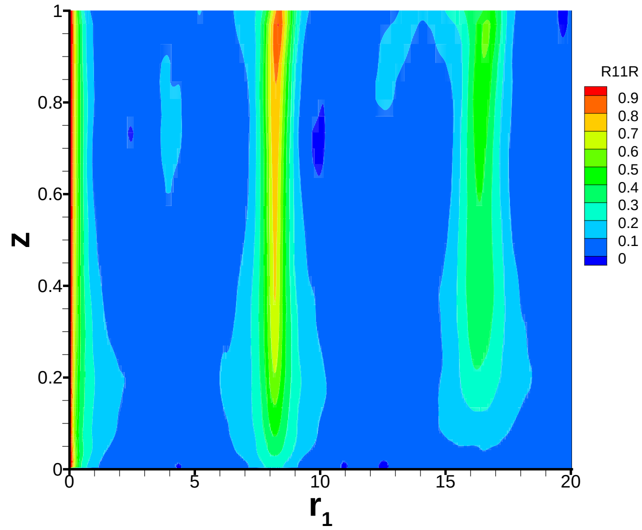

Figure 2.2: R_{11} contour on a $x_1 - x_3$ plane at $Re_\theta = 1430$ without reflection.

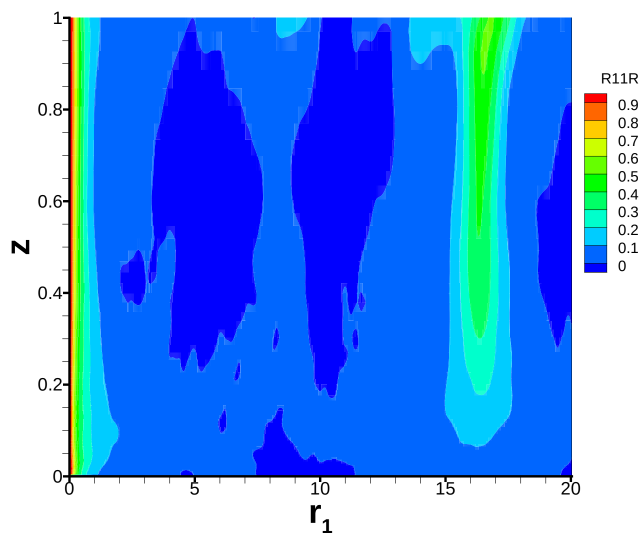

Figure 2.3: R_{11} contour on a $x_1 - x_3$ plane at $Re_\theta = 1430$ with the inflow plane reflected.

Case	λ_{rfl}
1	1.25 ± 0.25
2	2.5 ± 0.5
3	5 ± 1
4	7.5 ± 1.5

Table 2.2: Dynamic reflection parametric study

in Fig. 2.4. A comparison of the mean velocity profile and velocity correlations to experimental data from De Graaff & Eaton (2000) and DNS data from Schlatter *et al.* (2010) is provided in Fig. 2.5. This shows that the disruption of the vortical structures by dynamic reflection does not affect the turbulence statistics.

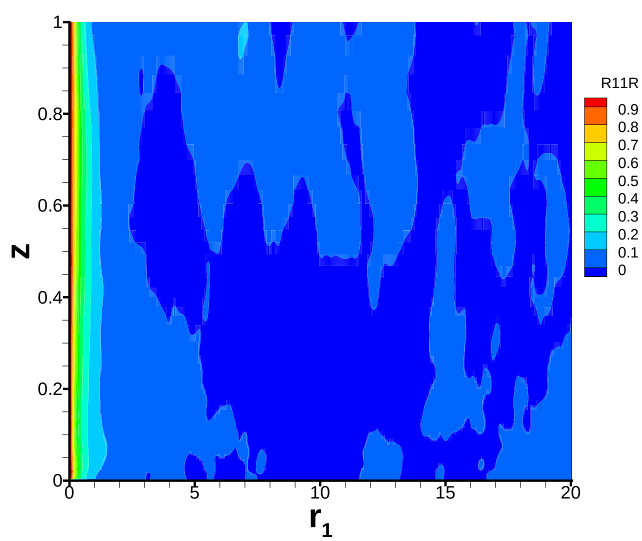

Figure 2.4: R_{11} contour on a $x_1 - x_3$ plane with the inflow dynamically reflected.

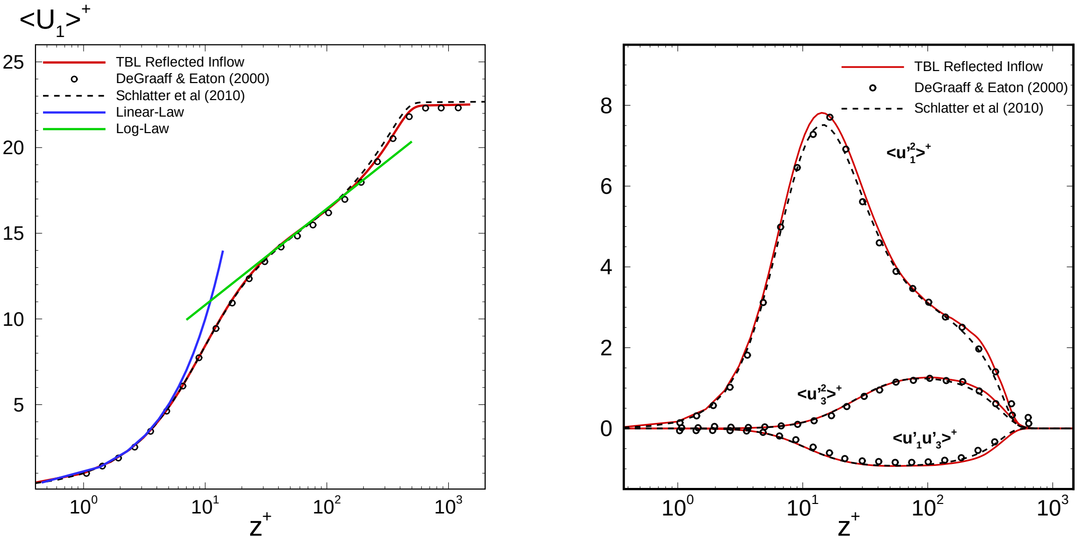

Figure 2.5: Mean velocity profile (a) and velocity correlation (b) comparisons of the DNS code with dynamic reflection (Case C) to experiments by De Graaff & Eaton (2000) and DNS data by Schlatter *et al.* (2010) at $Re_\theta = 1430$.

2.3.2 Outflow Boundary Condition

At the outflow plane ($x = L_x$) the following convective condition by Lowery & Reynolds (1987) was imposed for the velocity components,

$$\frac{\partial u_j}{\partial t} + U_c \frac{\partial u_j}{\partial x} = 0. \tag{2.7}$$

where U_c is the convective velocity at the exit plane and u_j is the instantaneous velocity in the stream-wise direction in which the reference velocity is subtracted ($U_1(x,y,z,t) = U_{ref}(z) + u_1(x,y,z,t)$). The convective velocity in Ferrante & Elghobashi (2004a) was defined by averaging the convective velocity (2.8) in the span-wise and wall-normal directions:

$$U_C(t) = \langle\langle U_C(x,y,z,t)\rangle_y\rangle_z \tag{2.8}$$

The new outflow convective velocity (2.9) is only averaged in the span-wise direction to preserve the wall-normal velocity profile:

$$U_C(z,t) = \langle U_C(x,y,z,t) \rangle_y \tag{2.9}$$

A zero-pressure gradient in the stream-wise direction ($\partial p/\partial x = 0$) is also imposed at the outflow plane.

Differences between the two outflow boundary conditions (2.8) and (2.9) can clearly be see in Fig. (2.7). The average velocity in the wall normal direction is $U_c \sim 0.8U_\infty$ shown in Fig. (2.6). This simplification causes the flow above the boundary layer to slow and the flow near the wall to artificial increase near the outlet. With most of the grid points contained within the boundary layer due to the grid stretching in the wall normal direction, the Reynolds number spuriously increases near the outlet. This can be seen with the solid black line. Removing the wall normal average from U_C allows for the changes in the stream-wise velocity to be properly modeled. As seen in Fig. (2.7), the Reynolds number no longer has the large increase near the outflow plane.

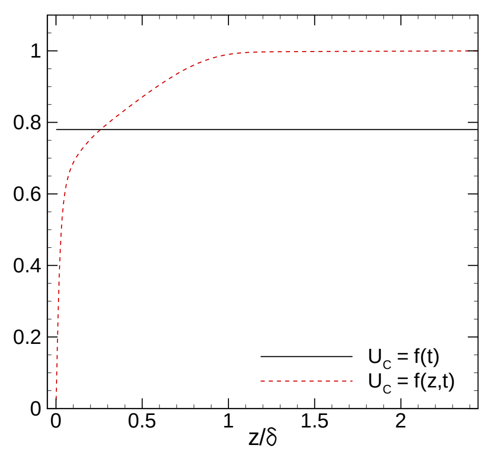

Figure 2.6: Convective velocities for (2.8) and (2.9), denoted by the solid and dashed lines respectively

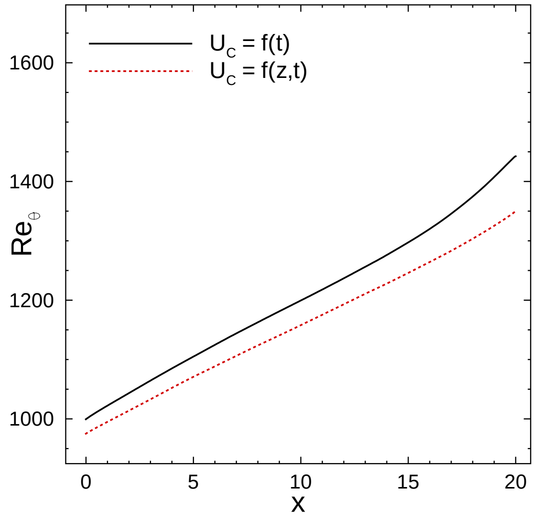

Figure 2.7: Reynolds number versus x for outflow boundary conditions (2.8) and (2.9), denoted by the solid and dashed lines respectively

Chapter 3
RESULTS

3.1 Mesh Refinement

Comparing the Reynolds stress $\langle u_1^2 \rangle^+$ to experimental data from De Graaff & Eaton (2000) reveals a large difference in the peak value as well as a lack of near wall resolution (Fig. 3.1). This difference was the motivation for mesh refinement.

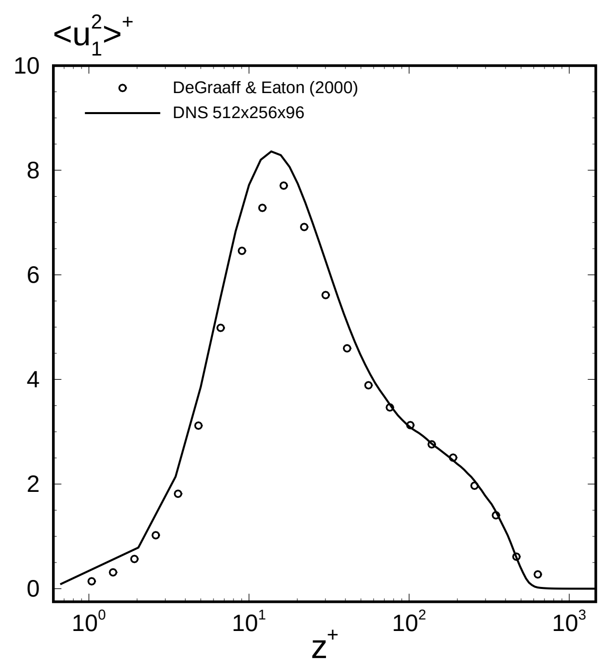

Figure 3.1: Stream-wise velocity fluctuation correlation for DNS and experimental data by De Graaff & Eaton (2000). at $Re_\theta = 1430$

The number of mesh points were doubled all three dimensions from (512x256x96) in the stream-wise, span-wise and wall normal directions respectively to (1024x512x192) grid points for $Re_\theta = 1430$. Reducing the grid spacing to $\Delta x^+ = 7$, $\Delta y^+ = 3.5$ and $\Delta z^+_{min} = 0.34$. Fig. 3.2 shows the improvement of the DNS solution after mesh refinement. Near the wall the refined mesh matches much more closely to the experimental data. At the peak around $z^+ = 10$ the value is reduced as the mesh is refined to match closely with the experiments. Fig. 3.3 shows an improvement near the wall for the mean stream-wise velocity profile.

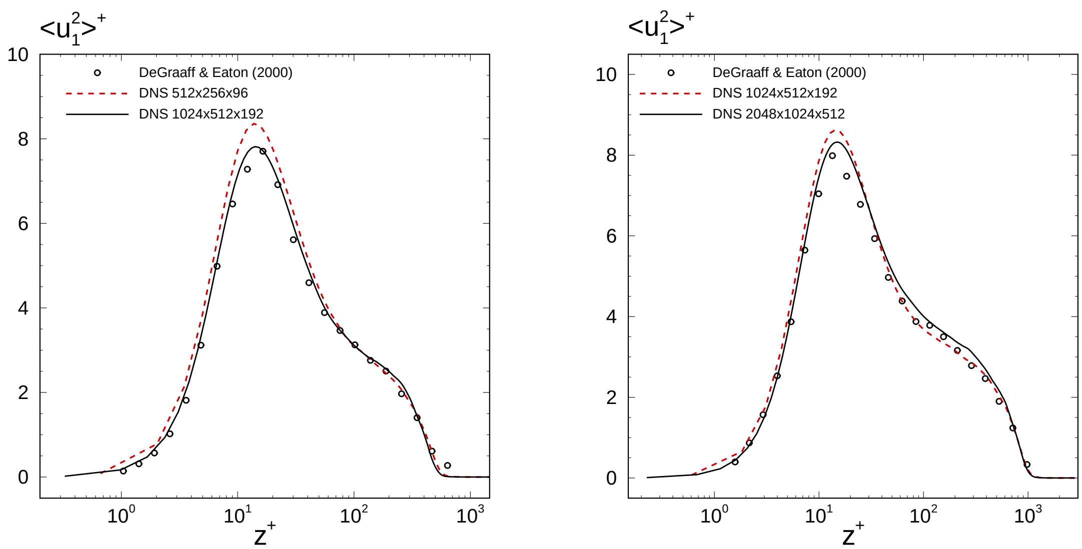

(a) $Re_\theta = 1430$ (b) $Re_\theta = 2900$

Figure 3.2: $\langle u_1'^2 \rangle^+$ Reynolds stress for both experimental data by De Graaff & Eaton (2000) and DNS data.

We also checked the one-dimensional energy spectra $E_{ij}(\kappa_1)$ where κ_1 is the wave number and R_{ij} is the temporal autocovariance:

$$E_{ij}(\kappa_1) = \frac{1}{\pi}\int_{-\infty}^{\infty} R_{ij}(\mathbf{e}_1 r_1) e^{i\kappa_1 r_1} \tag{3.1}$$

If the highest wave numbers (corresponding to Kolmogorov length scale have not been resolved, the energy cascade interrupts at the highest resolved wave-number. Thus the energy accumulates at this wave number and can affect the rest of the spectrum

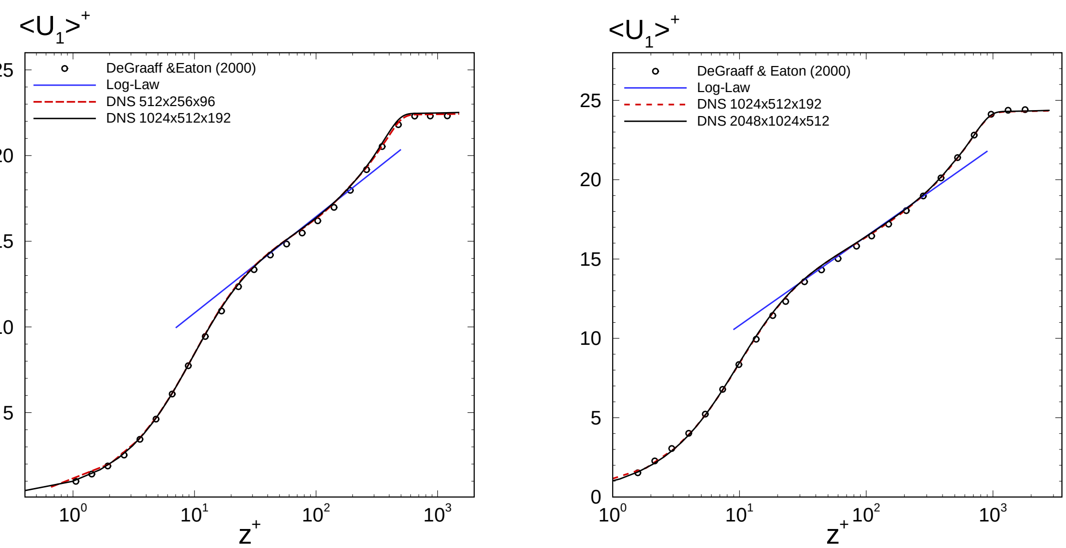

(a) $Re_\theta = 1430$

(b) $Re_\theta = 2900$

Figure 3.3: Mean stream-wise velocity profiles comparison of experiments by De Graaff & Eaton (2000), the log-law $[\langle U\rangle^+ = \frac{1}{0.41}\log(z^+) + 5.2]$ and DNS data at two different Reynolds numbers.

as shown by the red lines in Fig. (3.4), whereas the black lines (higher resolution) decay at high wave numbers.

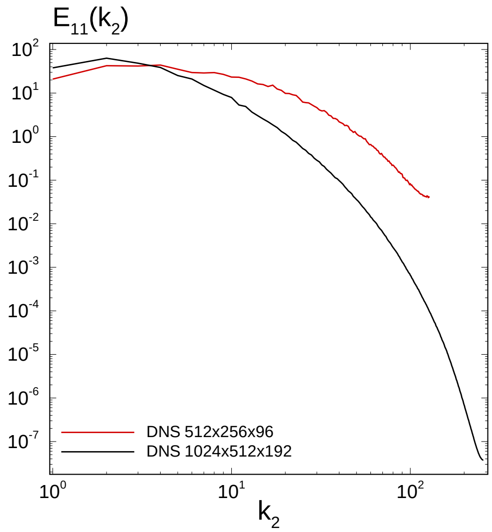

(a) E_{11}

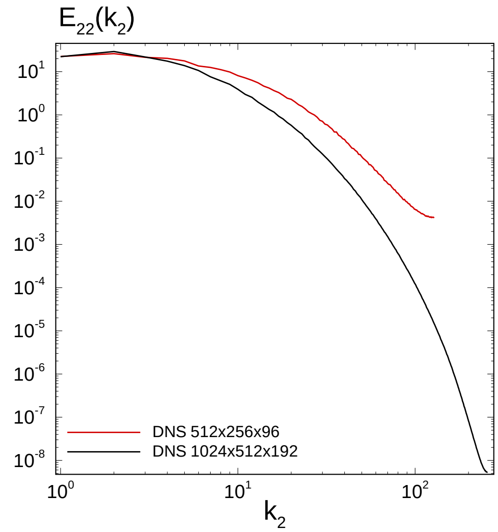

(b) E_{22}

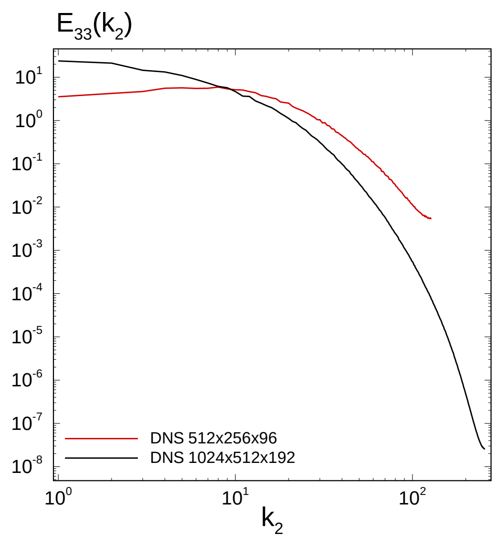

(c) E_{33}

Figure 3.4: Energy spectra for the stream-wise, span-wise and wall-normal directions with a fine and coarse mesh.

3.2 Reynolds Stresses

The Reynolds stress equation is given as equation is (Pope (2000)):

$$\frac{\overline{D}}{\overline{D}t}\langle u_i u_j \rangle = -\frac{\partial}{\partial x_k}\langle u_i u_j u_k \rangle + \nu \nabla^2 \langle u_i u_j \rangle + \mathcal{P}_{ij} + \Pi_{ij} - \epsilon_{ij}, \tag{3.2}$$

where the mean material derivative of the Reynolds stress tensor is

$$\frac{\overline{D}}{\overline{D}t}\langle u_i u_j \rangle \equiv \frac{\partial \langle u_i u_j \rangle}{\partial t} + \langle U_i \rangle \frac{\partial \langle u_i u_j \rangle}{\partial x_i}, \tag{3.3}$$

the turbulent convection tensor is

$$-\frac{\partial}{\partial x_k}\langle u_i u_j u_k \rangle, \tag{3.4}$$

the diffusion tensor is

$$\nu \nabla^2 \langle u_i u_j \rangle, \tag{3.5}$$

the production tensor is

$$\mathcal{P}_{ij} \equiv -\langle u_i u_k \rangle \frac{\partial \langle U_j \rangle}{\partial x_k} - \langle u_i u_k \rangle \frac{\partial \langle U_i \rangle}{\partial x_k}, \tag{3.6}$$

the velocity-pressure-gradient tensor (pressure transport) is

$$\Pi_{ij} \equiv -\frac{1}{\rho}\left\langle u_i \frac{\partial p'}{\partial x_j} + u_j \frac{\partial p'}{\partial x_i} \right\rangle, \tag{3.7}$$

and the dissipation tensor is

$$\epsilon_{ij} \equiv 2\nu \left\langle \frac{\partial u_i}{\partial x_k}\frac{\partial u_j}{\partial x_k} \right\rangle. \tag{3.8}$$

Appendix A shows a comparison of TBL Reynolds stresses at $Re_\theta = 1410$ and 2540 compared to DNS data from Spalart (1988) and Schlatter *et al.* (2010) to verify the statistics. The statistics provided by Schlatter *et al.* (2010) are taken with a longer time average, giving smoother statistics than the data from the TBL code and Spalart (1988), but the trends are still clear in all three data sets. Though the magnitudes differ slightly, the overall trends and peak locations are in agreement for all three data sets.

Fig. 3.5 shows the total turbulent kinetic energy (TKE) balance at $Re_\theta = 1430$ and 2900 with two different normalizations. (a) is normalized as a function of z so that the sum of the squares of the terms equals one. This shows the dominant terms at a given wall-normal location. (b) is normalized by the viscous scales ($\frac{u_\tau^3}{\partial_\nu}$) and shows the near-wall region.

At the near-wall region, Fig. 3.5(b), there is little difference between at the two different Reynolds numbers. Within the viscous sub-layer the terms appear to overlap with the exception of the dissipation, which increases with Reynolds number. Farther out the within the buffer layer the dissipation and turbulent convection terms increase and decrease in magnitude respectively.

In Fig. 3.5(a), the difference is more noticeable. The budget terms rise sharply and reach a peak values closer to the wall and decrease more precipitously for $Re_\theta = 2900$. Showing that at increasing the Reynolds number draws this peak in the budget term magnitudes closer to the wall . Further out from the wall, the opposite appears to be true. At $Re_\theta = 1430$ the terms rise or fall closer to the wall than $Re_\theta = 2900$. Such that the budget terms keep the same shape, but appear to be stretched. So that at the near-wall the changes happen closer to the wall, but away from the wall the terms rise or decay further from the wall as Reynolds number increases.

Fig. 3.6 and 3.7 show the normal and shear-stress balances at $Re_\theta = 1430$ and 2900 with normalization (a) and (b) respectively. It can be seen that $\langle u^2 \rangle$ is the only source of kinetic energy production for the normal stresses, which is balance by the dissipation and pressure terms until around $z/\delta \simeq 0.7$ when turbulent convection and mean convection become dominant. $\langle u^2 \rangle$ is the largest stress and accounts for most of the total TKE budget.

Near the wall $\langle u^2 \rangle$ is virtually the same at both Reynolds numbers, except for an increase in the pressure transport term. $\langle v^2 \rangle$ and $\langle w^2 \rangle$ show large increases in the pressure transport and dissipation terms. This shows that as Reynolds number is increased, there is an increase in TKE dissipation in the span-wise and wall normal directions. There is also increase in the pressure transport in all three spatial dimensions.

Overall, near the wall there appears to only be small changes in the total TKE budget. Looking away from the wall the TKE terms are stretched to the near-wall and past $z = \delta$. A third higher Reynolds number is needed to quantify and validate these trends.

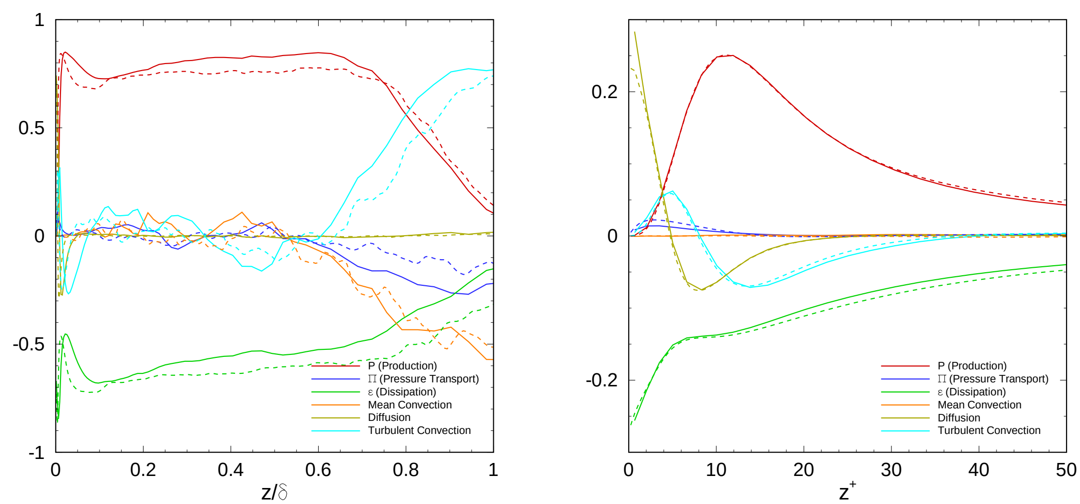

(a) (b)

Figure 3.5: Total TKE budget comparison of the TBL code at $Re_\theta = 1430$ and 2900 as solid and dashed lines respectively. (a) Normalized as a function of z with the sum of the squares of the terms equal to one. (b) Normalized by the viscous scales.

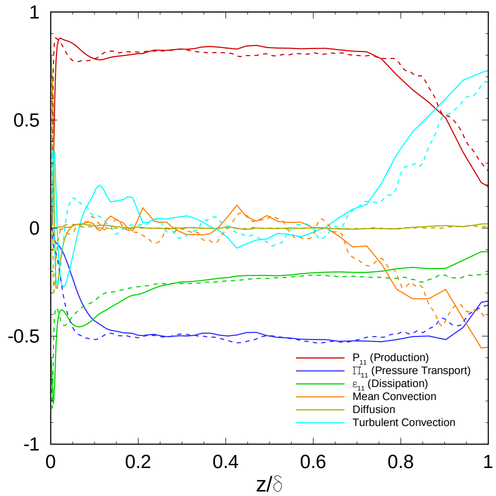

(a) $\langle u^2 \rangle$ budget

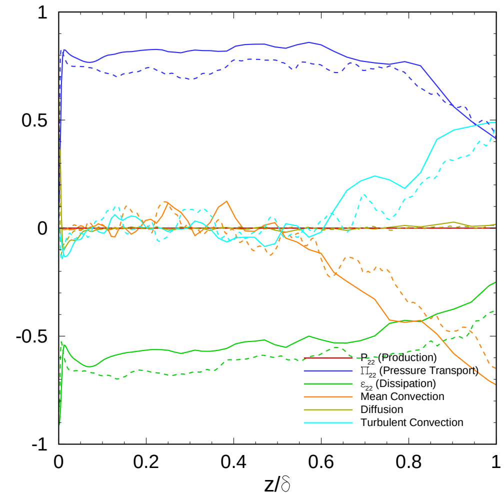

(b) $\langle v^2 \rangle$ budget

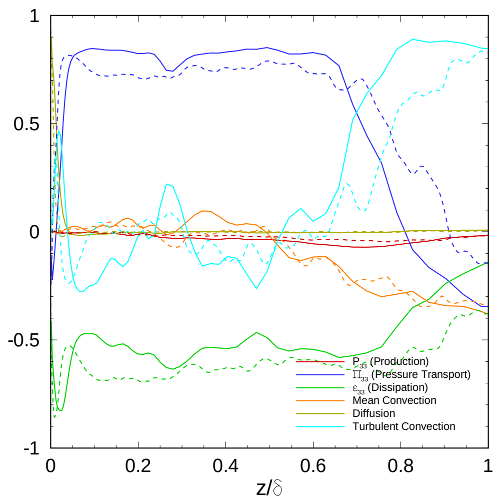

(c) $\langle w^2 \rangle$ budget

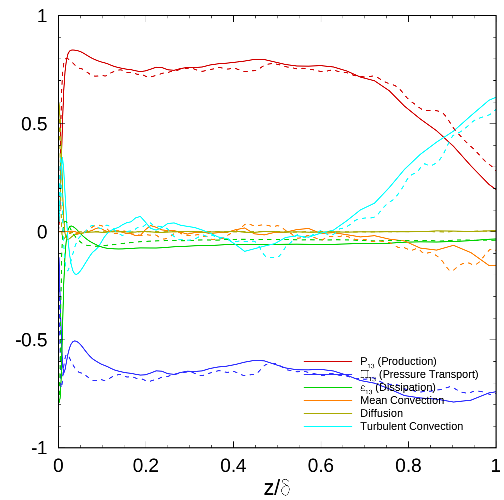

(d) $\langle uw \rangle$ budget

Figure 3.6: The TKE budget comparison of the TBL code at $Re_\theta = 1430$ and 2900 as solid and dashed lines respectively. Normalized as a function of z with the sum of the squares of the terms equal to one.

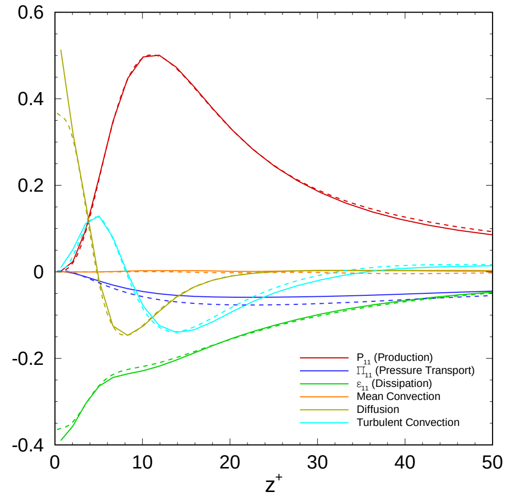

(a) $\langle u^2 \rangle$ budget

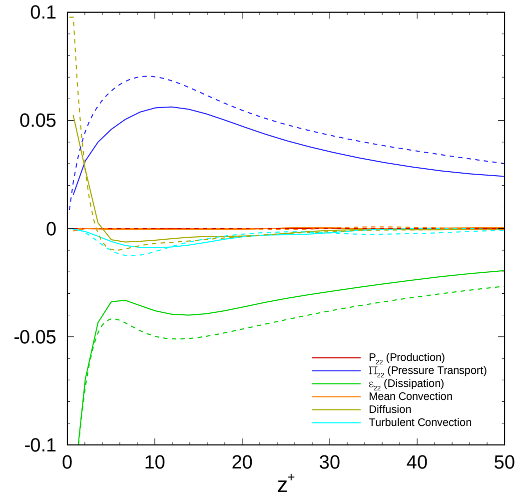

(b) $\langle v^2 \rangle$ budget

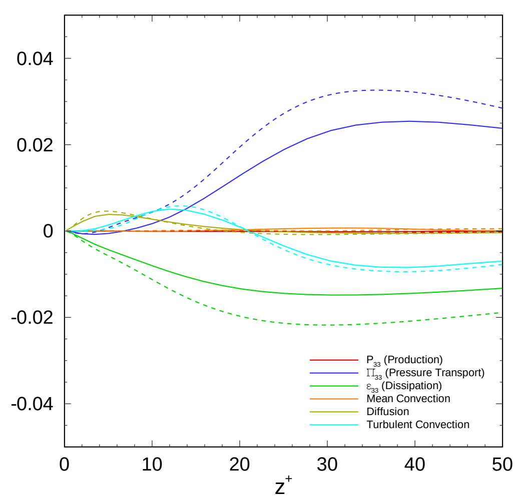

(c) $\langle w^2 \rangle$ budget

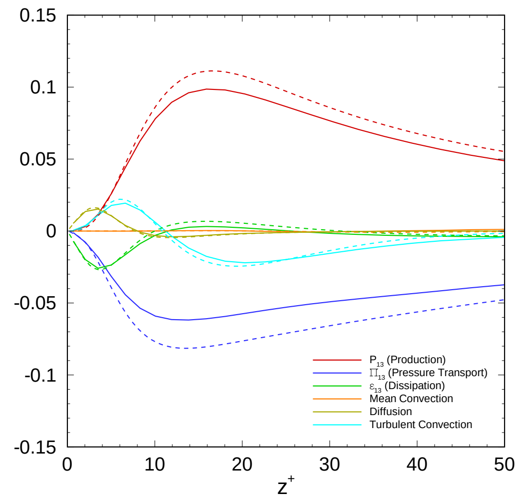

(d) $\langle uw \rangle$ budget

Figure 3.7: The TKE budget comparison of the TBL code at $Re_\theta = 1430$ and 2900 as solid and dashed lines respectively. Normalized by the viscous scales.

Figure 3.8 $\langle U_1 \rangle^+$ vs. z^+ at $Re_\theta = 1430$ and 2900. As expected, there is an increase in the the $\langle U_1 \rangle^+$ peak due to the decrease in u_τ. The inner layer is primarily dominated by viscous forces whereas the outer layer is dominated by inertial forces. An overlap of the inner and outer layers occurs at high Reynolds numbers. At $Re_\theta = 1430$ there is a small overlap of the inner and outer layers. $Re_\theta = 2900$ shows an increase in the overlap region where both viscous and inertial forces are important. Another trend as Reynolds number increases is that the log-layer region expands further into the outer layer. From $Re_\theta = 1430$ to 2900, the log-layer region has doubled in size.

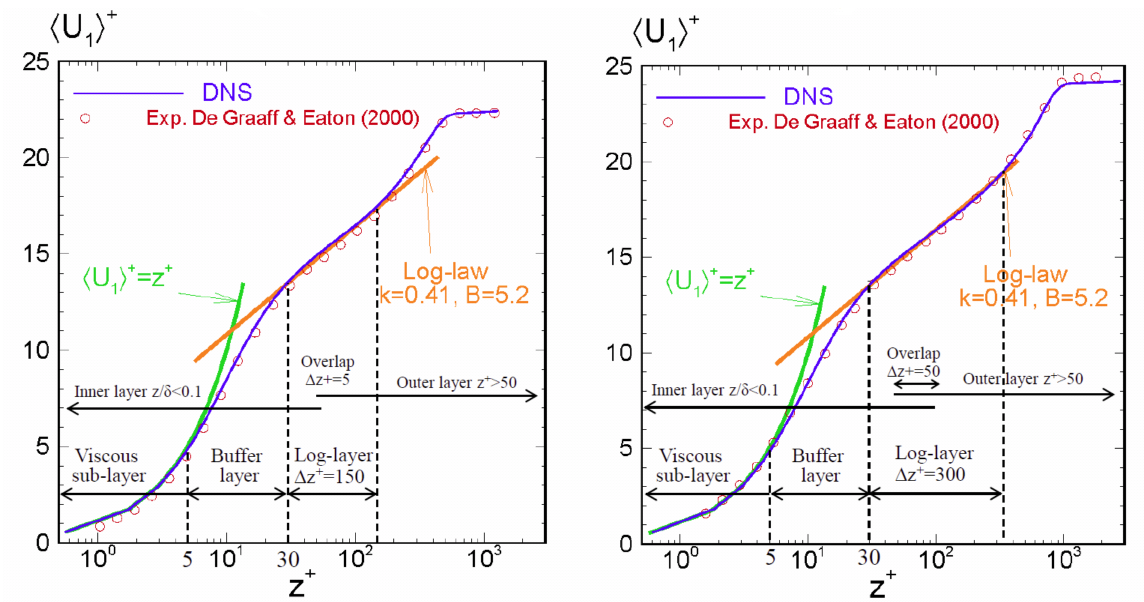

Figure 3.8: Mean stream-wise velocity profiles at $Re_\theta = 1410$ and 2900 from left to right with experimental data from De Graaff & Eaton (2000) and the TBL DNS data.

Chapter 4

CONCLUSIONS AND FUTURE RESEARCH

Modifications were made to the TBL code in order to improve the codes performance and the accuracy of the turbulence statistics. Code-A Task-1 was replaced by interpolation of lower Reynolds number velocity fields to be used as initial conditions for higher Reynolds number simulations. This saved thousands of computational hours and allows the code to be run at higher Reynolds numbers. Additionally Code-A Task-2 and Code-B were combined into a single simulation reducing the computational time by half.

The inflow recycling/rescaling method was modified based on the paper by Morgan *et al.* (2011) to remove spurious velocity correlations in the streamwise direction. This was done by adding dynamic reflection to the inflow plane to decorrelate the flow. A parametric study was done to find the optimal time between reflections to remove the spurious correlations while not affecting the turbulence statistics. The outflow boundary condition was modified to preserve the wall-normal velocity profile of the outflow convective velocity. This removed the non-physical increase of the Reynolds number near the outflow boundary.

Looking at the one-dimensional energy spectrum and comparing the Reynolds stresses and mean stream-wise velocity profile $\langle U_1 \rangle^+$ to experiments justified a need for mesh refinement. Doubling the number of grid-points in all three spatial dimensions added more accuracy of $\langle U_1 \rangle^+$ in the viscous sub-layer and improved the peak of $\langle u_1^2 \rangle^+$.

In order to improve LES subgrid-scale models, full Reynolds stress statistics were added to the TBL code. Near the wall, the Reynolds stress terms normalized by viscous scales stay relatively the same as Reynolds number is increased. Away from the near wall, the terms are pulled towards the wall and the top of the boundary layer. An third simulation at a higher Reynolds number ($Re_\theta = 5200$) is needed to confirm this trend and predict what will happen at even higher Reynolds numbers.

Work was started on converting the TBL code from 1-D domain decomposition to 2-D for multicore parallel computing, discussed in detail in Appendix B. Conversion to 2-D domain decomposition is near completion allowing for simulations at Reynolds numbers greater than 5200, eliminating the need for additional processors allocated for memory, and going from terascale computing using $O(10^3)$ cores to petascale computing using $O(10^5, 10^6)$ cores.

Simulations were performed in collaboration with David Bock to produce visualizations reported in Appendix C. The purpose of these visualizations is to investigate whether bottom-up or top-down mechanisms become more prevalent as Reynolds number increases.

BIBLIOGRAPHY

Bake, S., Meyer, D. & Rist, U. 2002 Turbulence mechanism in klebanoff transition: a quantitative comparison of experiment and direct numerical simulation. *Journal of Fluid Mechanics* **459**, 217–243.

De Graaff, D. B. & Eaton, J. K. 2000 Reynolds-number scaling of the flat-plate turbulent boundary layer. *Journal of Fluid Mechanics* **422** (1), 319–346.

Dodd, M. S., Webster, K. & Ferrante, A. 2012 Direct numerical simulation of particle dispersion in a spatially developing turbulent boundary layer. *Seventh International Conference on Computational Fluid Dynamics (ICCFD7)* .

Ferrante, A. & Elghobashi, S. 2004a A robust method for generating inflow conditions for direct simulations of spatially-developing turbulent boundary layers. *Journal of Computational Physics* **198** (1), 372–387.

Ferrante, A., Elghobashi, S., Adams, P., Valenciano, M. & Longmire, D. 2004b Evolution of quasistreamwise vortex tubes and wall streaks in a bubble-laden turbulent boundary layer over a flat plate. *Physics of Fluids* **16** (9), S2–S2.

Li, N. 2013 Library for 2d pencil decomposition and distributed fast fourier transform. `http://www.2decomp.org/decomp.html`, accessed: 2013-12-04.

Lowery, P. S. & Reynolds, W. C. 1987 Numerical simulation of a spatially-developing, forced, plane mixing layer. PhD thesis, Stanford University.

Lund, T. S., Wu, X. & Squires, K. D. 1998 Generation of turbulent inflow data for spatially-developing boundary layer simulations .

Morgan, B., Larsson, J., Kawai, S. & Lele, S. K. 2011 Improving low-frequency characteristics of recycling/rescaling inflow turbulence generation. *AIAA journal* **49** (3), 582–597.

Perry, A., Lim, T. & Teh, E. 1981 A visual study of turbulent spots. *Journal of Fluid Mechanics* **104** (1), 387–405.

Pope, S. B. 2000 *Turbulent flows*. Cambridge university press.

Schlatter, P., Li, Q., Brethouwer, G., Johansson, A. V. & Henningson, D. S. 2010 Simulations of spatially evolving turbulent boundary layers up to reθ= 4300. *International Journal of Heat and Fluid Flow* **31** (3), 251–261.

Spalart, P. R. 1988 Direct simulation of a turbulent boundary layer up to re_θ = 1410. *Journal of Fluid Mechanics* **187** (1), 61–98.

Appendix A

REYNOLD STRESSES VERIFICATION

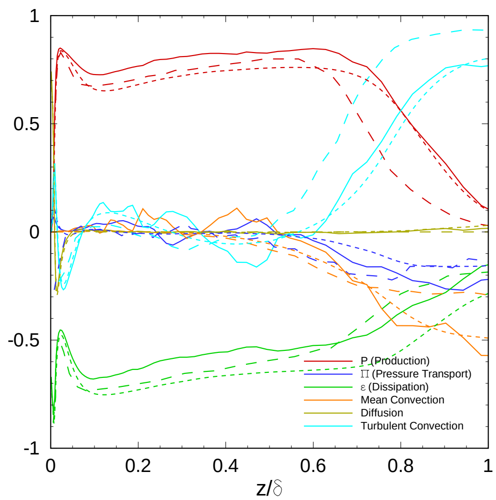

(a)

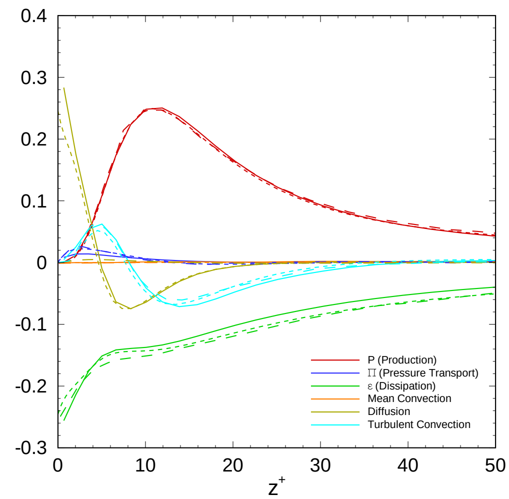

(b)

Figure A.1: Total TKE budget at $Re_\theta = 1410$. The TBL code (solid line) is compared to DNS data from Spalart (1988) (long-dash lines) and Schlatter *et al.* (2010) (short-dash lines). (a) Normalized as a function of z with the sum of the squares of the terms equal to one. (b) Normalized by the viscous scales.

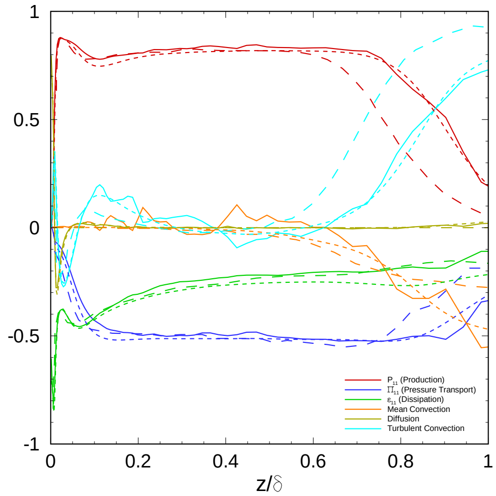

(a) $\langle u^2 \rangle$ budget

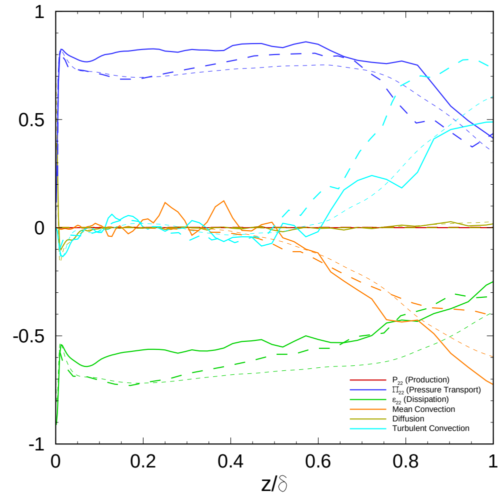

(b) $\langle v^2 \rangle$ budget

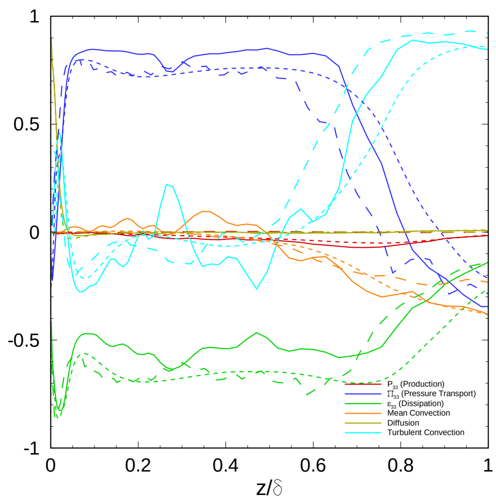

(c) $\langle w^2 \rangle$ budget

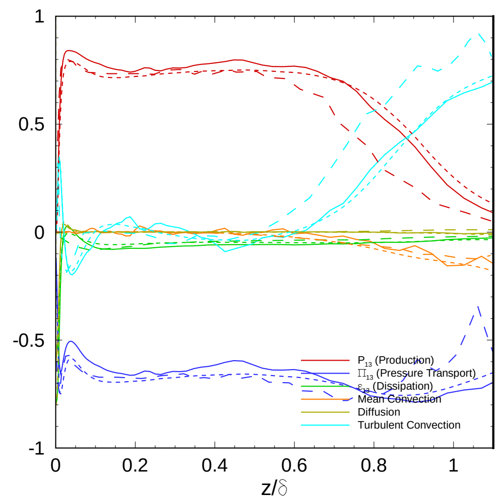

(d) $\langle uw \rangle$ budget

Figure A.2: The TKE budget at $Re_\theta = 1410$. The TBL code (solid line) is compared to DNS data from Spalart (1988) (long-dash lines) and Schlatter *et al.* (2010) (short-dash lines). Normalized as a function of z with the sum of the squares of the terms equal to one.

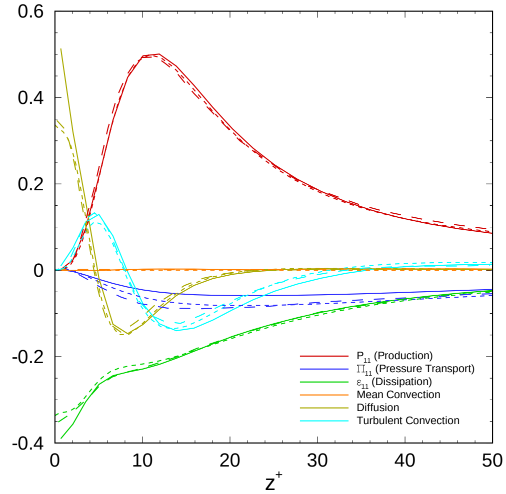

(a) $\langle u^2 \rangle$ budget

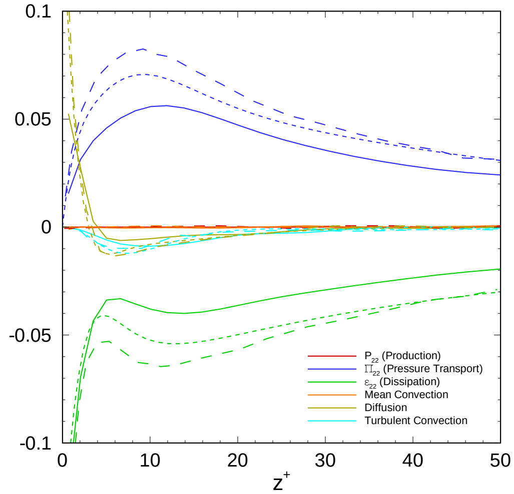

(b) $\langle v^2 \rangle$ budget

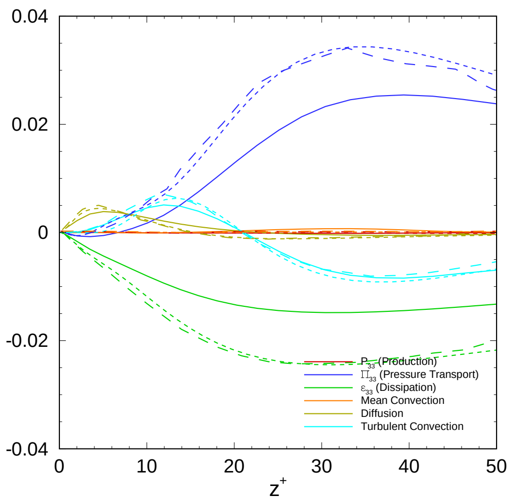

(c) $\langle w^2 \rangle$ budget

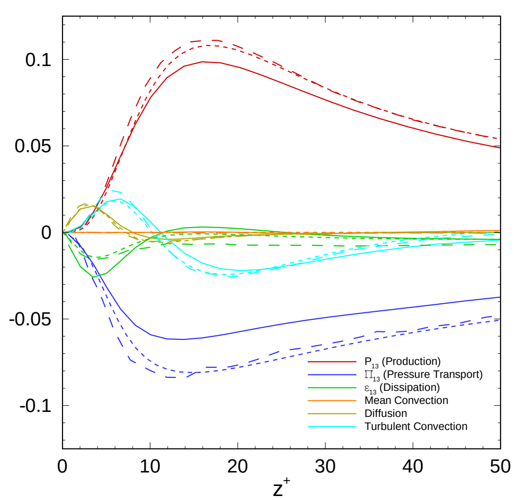

(d) $\langle uw \rangle$ budget

Figure A.3: The TKE budget at $Re_\theta = 1410$. The TBL code (solid line) is compared to DNS data from Spalart (1988) (long-dash lines) and Schlatter *et al.* (2010) (short-dash lines). Normalized by the viscous scales.

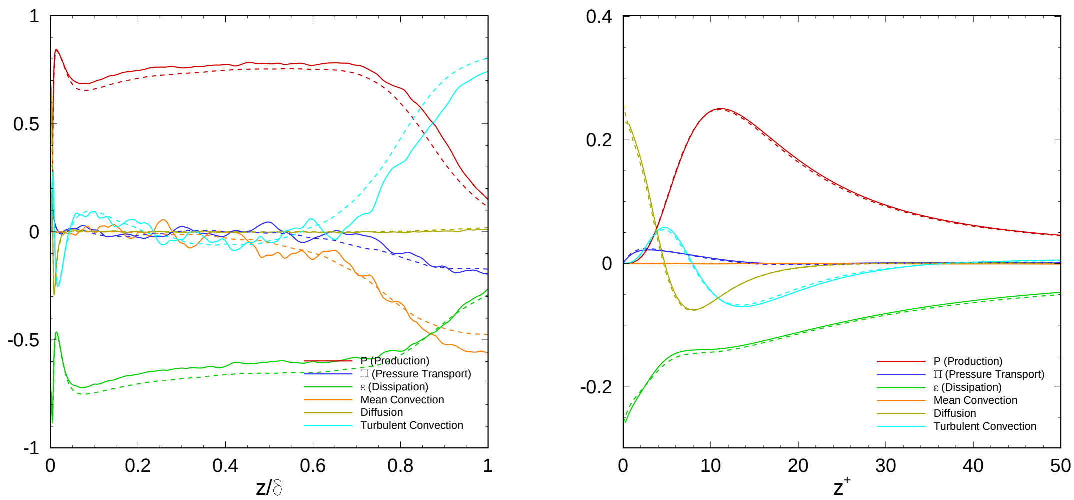

(a) (b)

Figure A.4: Total TKE budget at $Re_\theta = 2540$. The TBL code (solid line) is compared to DNS data from Schlatter *et al.* (2010) (dashed line). (a) Normalized as a function of z with the sum of the squares of the terms equal to one. (b) Normalized by the viscous scales.

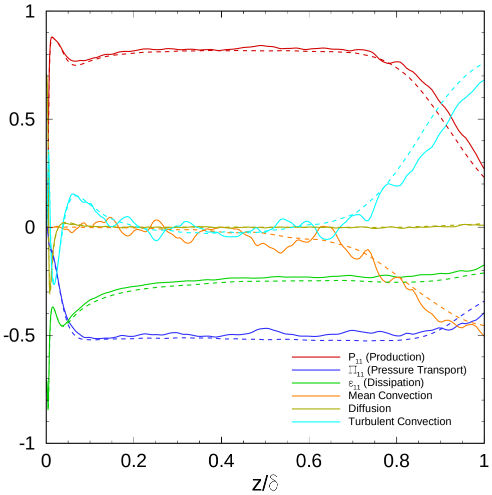

(a) $\langle u^2 \rangle$ budget

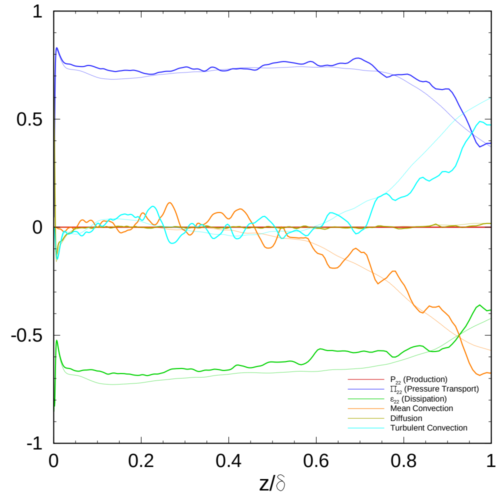

(b) $\langle v^2 \rangle$ budget

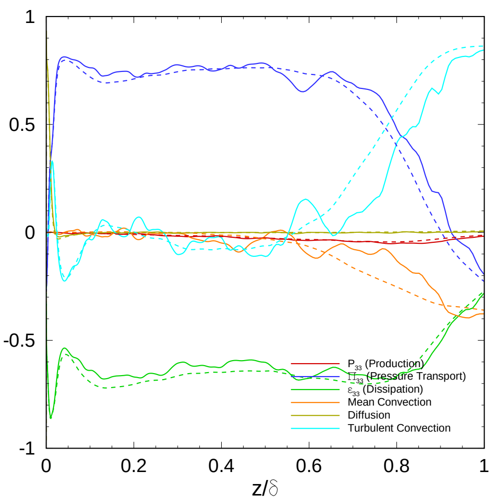

(c) $\langle w^2 \rangle$ budget

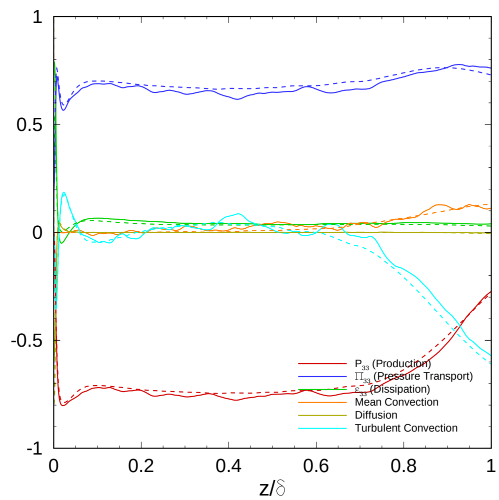

(d) $\langle uw \rangle$ budget

Figure A.5: The TKE budget at $Re_\theta = 2540$. The TBL code (solid line) is compared to DNS data from Schlatter *et al.* (2010) (dashed line). Normalized as a function of z with the sum of the squares of the terms equal to one.

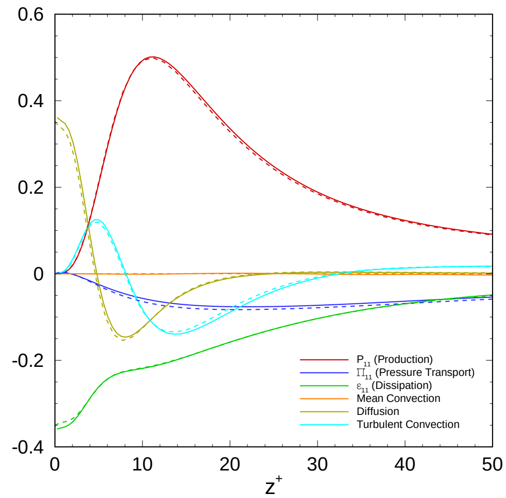

(a) $\langle u^2 \rangle$ budget

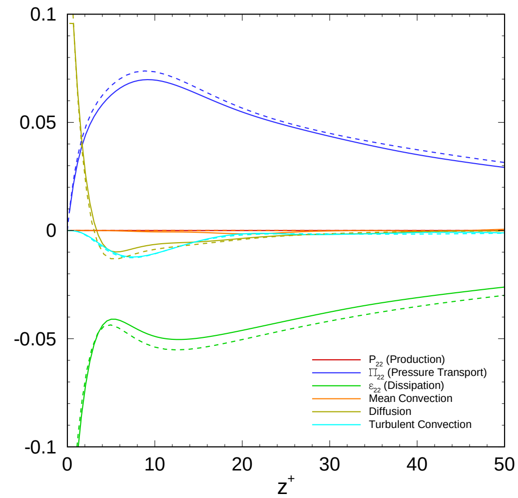

(b) $\langle v^2 \rangle$ budget

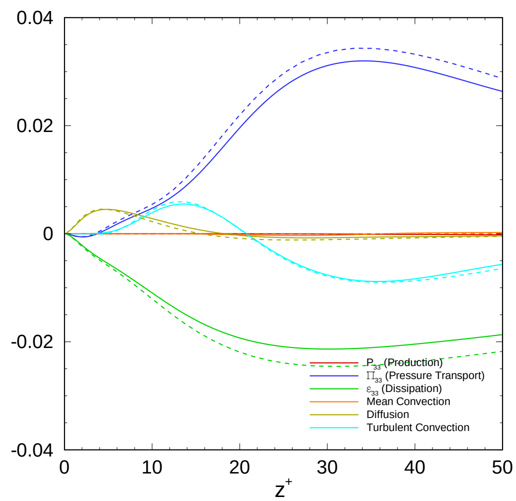

(c) $\langle w^2 \rangle$ budget

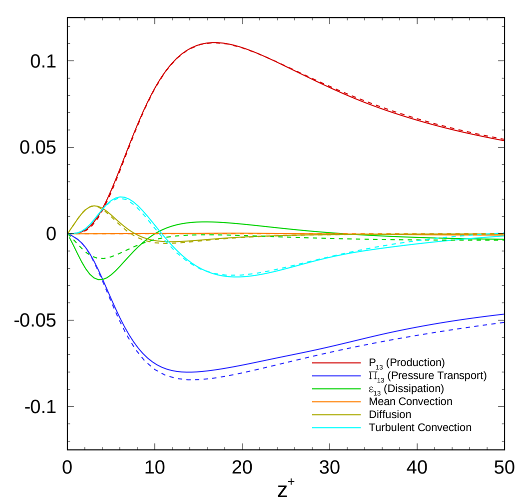

(d) $\langle uw \rangle$ budget

Figure A.6: The TKE budget at $Re_\theta = 2540$. The TBL code (solid line) is compared to DNS data from Schlatter *et al.* (2010) (dashed lines). Normalized by the viscous scales.

Appendix B
2-D DOMAIN DECOMPOSITION

The DNS code is currently being modified to run with 2-D domain decomposition. Currently the code is parallelized in the span-wise direction with each processor receiving a slab of the computational domain, using MPI to communicate between processors. The 1-D domain decomposition is limited by the fact that the number of processors must be divisible by the number of grid points in the span-wise direction. This limits the maximum number of processors. This was not a problem at lower Reynolds numbers (mesh of the order 10^7 grid points), but at $Re_\theta = 2900$ or higher, the simulation runs into memory issues and needs to call extra processors to use as additional memory. The $Re_\theta = 2900$ (2048x1024x512) run only uses a third of the processors for computation and the other two thirds are devoted to memory when running on Kraken (Cray XT5) at the National Institute for Computational Sciences.

The solution is to add parallelization in the wall-normal direction, such that each processor gets a pencil of the computational domain rather than a slab. Fig. B.1 illustrates the change from 1-D to 2-D domain decomposition as seen on the website by Li (2013). From 1-D to 2-D domain decomposition, the maximum number of cores that could be used in a simulation increases from N_y (O$\sim 10^3$) to N_yxN_z (O$\sim 10^6$), where N_y and N_z are the number of grid points in the $y-$ and $z-$direction, respectively. Basically, this extends the code capability from terascale to petascale computing. This eliminates the need for additional processors dedicated to memory by reducing the portion of the domain each processor receives. Preliminary test have shown that the DNS code wall-clock time scales nearly linearly with respect to the number of processors. So that the code will not suffer performance loss with the 2-D domain decomposition.

The majority of code has been extended to 2-D domain decomposition by our research group. Making the DNS code more efficient and allowing for higher Reynolds number simulations.

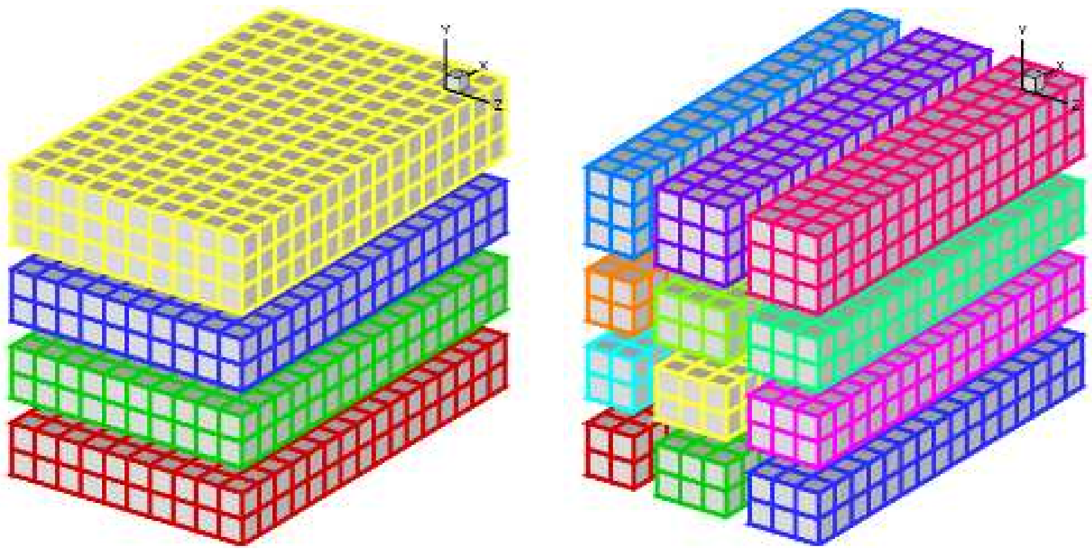

(a) (b)

Figure B.1: Illustration of (a) 1-D domain decomposition and (b) 2-D domain decomposition Li (2013).

Appendix C

VORTICAL STRUCTURES

Vortical structures visualizations were produced by David Bock by post-processing the NSF ASTA team at NCSA from the TBL DNS results.

Preliminary visualizations were created, shown in Fig. C.1 for $Re_\theta = 1430$ and 5200 using a Gaussian alpha transfer function to find the vortical structures. The vortical structures are identified as connected flow regions of negative values of λ_2, where λ_2 is the second largest eigenvalue of the tensor $(S_{ik}S_{kj} + \Omega_{ik}\Omega_{kj})$. $S_{ij} \equiv (\partial_j U_i + \partial_i U_j)/2$ is the strain-rate tensor and $\Omega_{ij} \equiv (\partial_j U_i - \partial_i U_j)/2$ is the rotation-rate tensor (Ferrante *et al.* (2004b)) The meshes used are (512x256x96) and (2048x1024x512) for $Re_\theta = 1430$ and 5200 respectively, i.e., half the grid points needed to fully resolve the flow in each spatial direction. As the Reynolds number increases, the vortical structures reduce in size and their number increases. Going from larger structures to many smaller structures. Fig. C.2 shows still frames from a recent video produced by David Bock with a mesh refined $Re_\theta = 1430$ run (1024x512x192) produced from the TBL code, which can be found at the website: `http://www.aa.washington.edu/research/cfm/videos.html`.

Figure C.3 shows hairpin-shaped vortical structures in the transition region from laminar to turbulent boundary layer from the paper by Perry *et al.* (1981). Also, Bake *et al.* (2002) show in simulations of Klebanoff transition to turbulence the existence of hairpin vortices. In the turbulence community there is still debate whether these hairpin vortices that occur at the transition to turbulence still exist at high Reynolds number flows. The present visualizations of TBL show vortical structures as elongated quasi-stream-wise tubes and arches in contrast with the hairpins seen

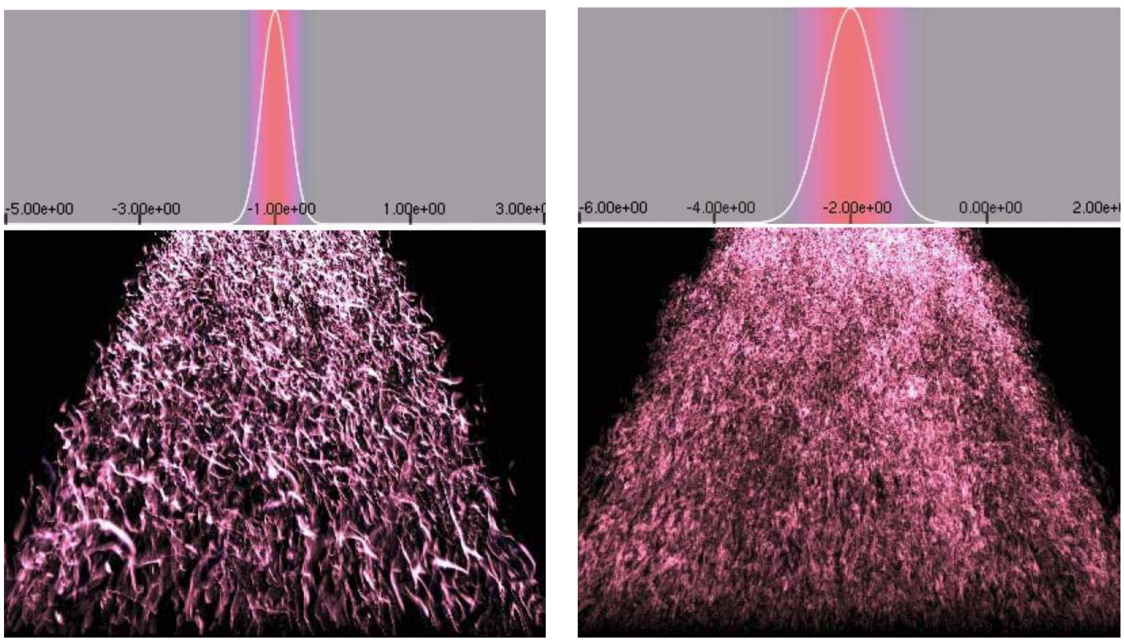

(a) (b)

Figure C.1: Coarse mesh vortical structures at $Re_\theta = 1430$ and 5200 with (512x256x96) and (2048x1024x512) meshes respectively

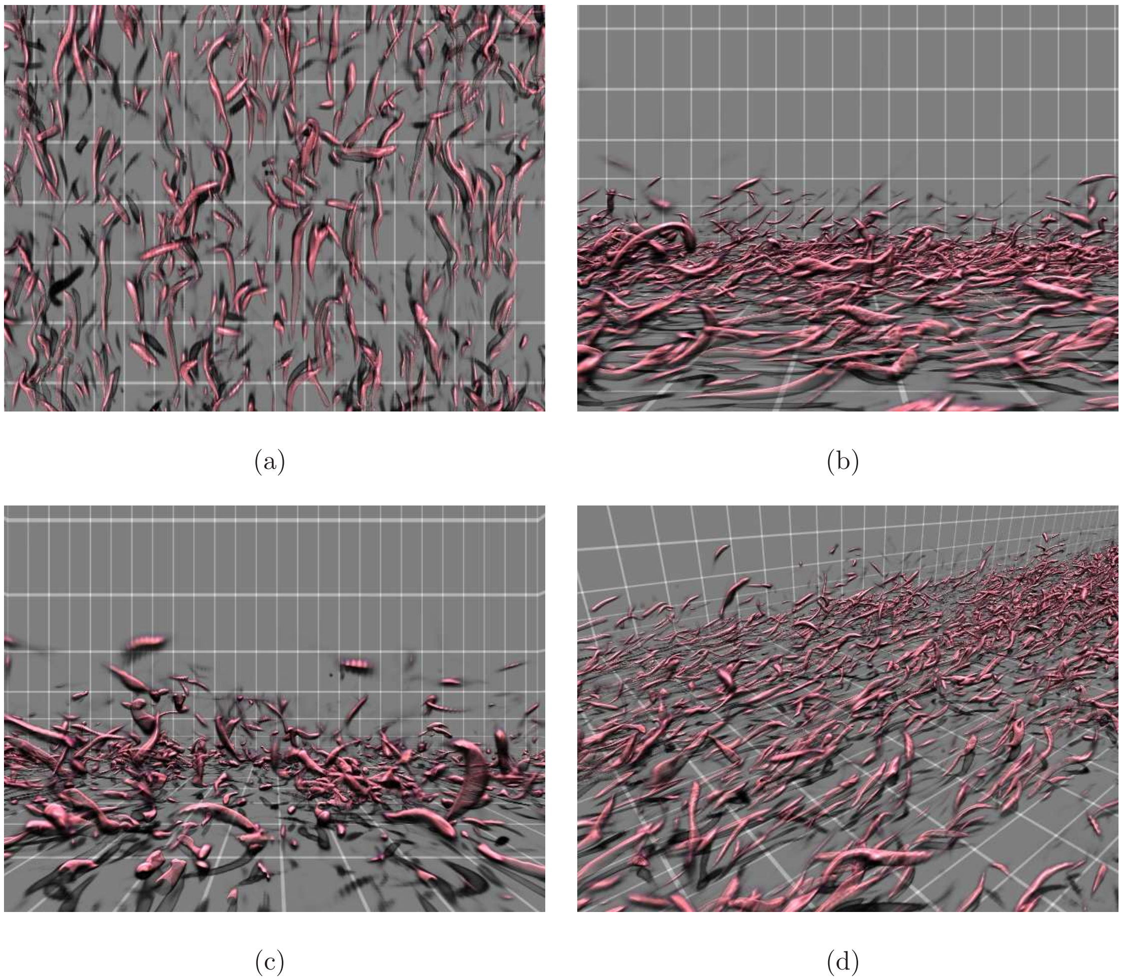

Figure C.2: Vortical structures at $Re_\theta = 1430$ (1024x512x192) viewed from the (a) top, (b) side, (c) outlet and (d) looking upstream.

in the transitional flow. Visualizations of data from $Re_\theta = 2900$ are currently being produced and, in the future, $Re_\theta = 5200$ will be run for visualizations.

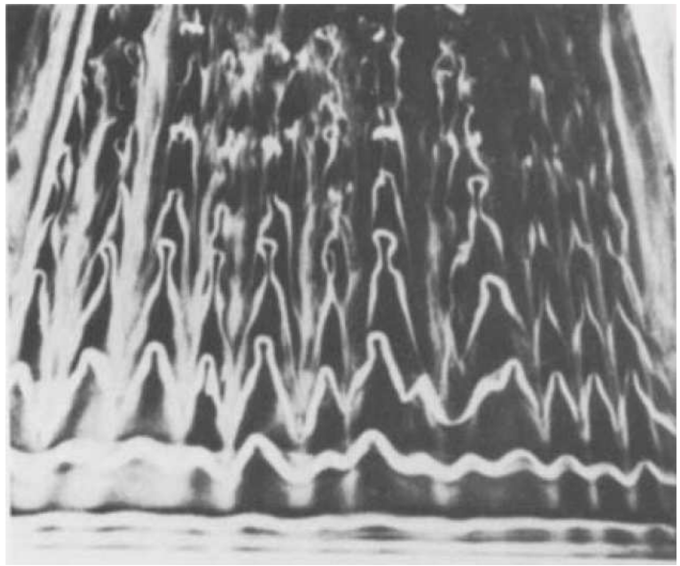

Figure C.3: Hairpin vortices developing in a boundary layer at the transition region from laminar to turbulent flow (Perry *et al.* (1981))